European Journal of Remote Sensing - 2014, 47: 537-556
doi: 10.5721/EuJRS20144730
Received 23/10/2013, accepted 04/06/2014

European Journal of Remote Sensing
An official journal of the Italian Society of Remote Sensing

www.aitjournal.com

InSAR decorrelation to assess and prevent volcanic risk

Eva Savina Malinverni[1]*, David T. Sandwell[2], Anna Nora Tassetti[1] and Lucia Cappelletti[1]

[1]DICEA, Engineering Faculty, Università Politecnica delle Marche,
via Brecce Bianche, 60100 - Ancona, Italy
[2]Scripps Institution of Oceanography, University of California,
San Diego, La Jolla, California, USA
*Corresponding author, e-mail address: e.s.malinverni@univpm.it

Abstract
SAR can be invaluable describing pre-eruption surface deformation and improving the understanding of volcanic processes. This work studies correlation of pairs of SAR images focusing on the influence of surface, climate conditions and acquisition band. Chosen L-band and C-band images (ENVISAT, ERS and ALOS) cover most of the Yellowstone caldera (USA) over a span of 4 years, sampling all the seasons. Interferograms and correlation maps are generated and studied in relation to snow depth and temperature. To isolate temporal decorrelation pairs of images with the shortest baseline are chosen. Results show good performance during winter, bad attitude towards wet snow and good coherence during summer with L-band performing better over vegetation.
Keywords: SAR, InSAR, correlation, risk prevention, volcanoes.

Introduction
A complex network of remote sensing satellites is nowadays orbiting around the earth, providing a huge quantity of information and various remote sensing techniques can be applied to study volcanic processes and detect precursory activity to volcanic hazards [Dzurisin, 2006; Di Martino et al., 2012]. In fact traditional ground deformation measurements, including levelling, have been integrated or even replaced by more advanced detection methodologies.
All imagery of eruptive activity is important to monitor progress of activity and more or less with good results. In recent decades two types of remote sensing techniques have in particular advanced: spectrometry and Synthetic Aperture Radar Interferometry (InSAR). The first puts forward in detecting eruption onset, mapping flows and deposit [Carter et al., 2009], monitoring volcanic eruption through detection of hot spots [Rothery et al., 2005] and quantifying the amount of ash and SO2 emitted in eruptive plumes [Ramsey and Flynn,

2004] and while InSAR in estimating ground deformation both on large and small scale [Massonnet and Feigl, 1998; Burgmann et al., 2000; Rosen et al., 2000]. He first application on InSAR to measure volcanic deformation was dealing with Mount Etna in 1995 [Massonnet et al., 1995]. For other volcanic applications, see Massonnet and Sigmundosson [2000] and Zebker et al. [2000]. In the last decade, two-pass InSAR was increasingly applied to volcanos. Works deal with inferred magma chambers and their inflation/deflation [Lu et al., 2000], sill and dike intrusion [Fukushima et al., 2005], eruption [Froger et al., 2004] etc.

In this paper we address this last type of remote sensing technique because invaluable to study volcanoes and the related natural hazards. The broad and detailed spatial coverage of radar satellites, giving continuous and accurate deformation data in time and space, provides important information on magma migration, pre-eruption surface deformation and other processes at depth improving the understanding of volcanic processes and hence, the ability to predict and understand eruptions. To play a key role are essentially GPS and SAR Interferometry: the first one gives continuous and accurate deformation data in time and the second one in space, covering in each image the volcano and its surrounding active area. As a downside, radar satellite measurements can be influenced by artifacts such as atmospheric effects or bad topographic data taken as reference. Correlation, sometimes called coherence, gives a measure of these interferences, quantifying the similarity of the phase of two SAR images.

Different approaches exist to reduce errors due to these artefacts but the main concern remain the possibility to correlate images with different acquisition times: snow-covered or heavily-vegetated areas produce seasonal changes on the surface. Sometimes in these conditions it is impossible to construct interferograms and assess ground deformations. The understanding of when and why two images have a sufficiently high coherence to generate an interferogram is important to extract all the expected deformation information. Generally, minimizing the time between passes partly limits decorrelation. Though, images of the area of interest with a short temporal baseline aren't always available and some artefacts affecting correlation are time-independent.

This work studies the correlation of pairs of SAR images covering the Yellowstone caldera, focusing on the influence of surface and climate conditions, especially snow coverage and temperature; furthermore, the effects of the acquisition band (the wavelength of the signal) on correlation are taken into account, comparing L-band and C-band images.

In the past few years the restless uplift and subsidence of this mega volcano has drawn the attention of scientists: the Yellowstone caldera has been the object of many studies and the InSAR technique has been largely used to detect its ground movements [Pelton and Smith, 1982]. All the chosen images/satellites (both ascending and descending) are selected considering the date of acquisition between a 4 years span (initially 1992-1996 and later also 2002-2006), possibly sampling all the seasons, and with an area covering most of the caldera. Results obtained with ENVISAT and ERS satellites (C band) are compared with the ones from ALOS (L-band) too. Interferograms and correlation maps are generated using the open source software GMTSAR developed by Sandwell et al. [2011] (http://topex.ucsd.edu/gmtsar/).

This work is organized as follows. Section 2 presents the study area while the Section 3 faces data and SAR technologies. Sections 4 and 5 discuss the applied procedures, the results and their comparison. The conclusion outlines some important remarks.

This research is realized with the support of IGPP Institute of Geophysics & Planetary Physics which designed the used InSAR processing system.

Study area

Yellowstone caldera

The study area is the Yellowstone caldera, inside the borders of the homonym National Park in the western United States, close to Idaho and Montana. The territory is mainly mountainous with peaks on the edges of the caldera reaching over 3000 meters and wide valleys where meadows are largely spread (Fig. 1). Forest covers most of the caldera and its surroundings, although open fire often hits the area leaving the bare ground to grass or to the slow growth of sporadic pine trees. The caldera, is the youngest part of the Yellowstone plateau, one of the most concentrated regions of magmatic, hydrothermal, and seismic activity in North America. The Plateau volcanic field formed during three major caldera-forming eruptions approximately 2.05, 1.3, and 0.63 Million years ago. The last explosive eruption ejected 1,000 km^3 of material, forming the current Yellowstone caldera. The following topographic map (Fig. 1) of the Yellowstone-Snake River plain shows Quaternary faults, historic earthquakes, and the locations of past caldera eruptions. Over the last 16 million years, there was a series of giant, caldera-forming eruptions, with the most recent at Yellowstone National Park 630,000 years ago [Smith and Siegel, 2000].

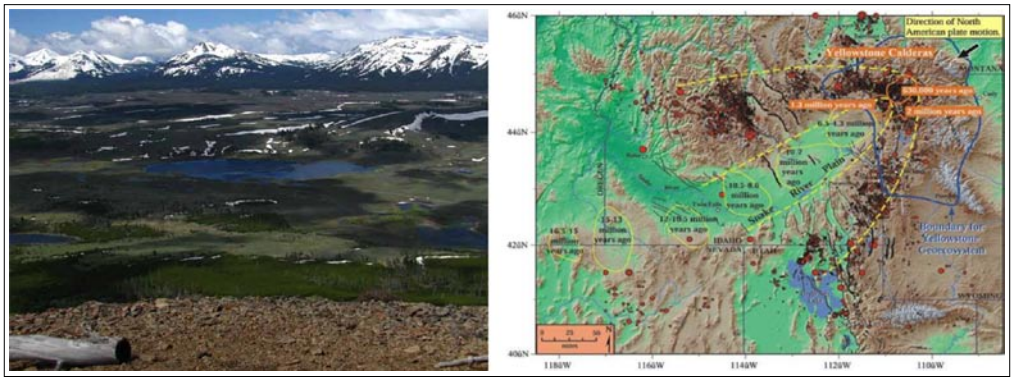

Figure 1 - The Yellowstone Park Area (left) and the Yellowstone-Snake River plain with hotspot's path (right).

Since the last eruption, Yellowstone has remained restless continuing uplift/ subsidence episodes with movements of 70 cm historically to several meters and intense hydrothermal activity. Due to this high seismicity, Yellowstone caldera has been always closely monitored: ground movements were first measured by surveyors and recently (two decades) with GPS stations and InSAR measurements [Meertens and Smith, 1991; Wei and Sandwell, 2010].

Caldera Crustal Deformation and geodetic monitoring

Yellowstone is an example of a giant caldera that has exhibited unprecedented caldera-wide deformation and has earned a reputation of a caldera at unrest, indeed a living, breathing caldera. Geodetic techniques including precise leveling, GPS (Global Positioning System), and InSAR (Interferometric Synthetic Aperture Radar) revealed multiple episodes of Yellowstone caldera uplift and subsidence from 1923 to 2003 with average rates of 1–2 cm/yr and unexpectedly high uplift rates up to 7 cm/yr through 2006 [Wicks et al., 2006; Chang

et al., 2007; Puskas et al., 2007]. In 2006 - 2008 uplift rates decreased from 7 to 5 cm/yr and 4 to 2 cm/yr in the northern and southwest caldera, respectively, and in 2009 rates further reduced to 2 cm/yr and 0.5 cm/yr in the same areas. Past episodes of uplift and subsidence in the caldera were attributed to various combinations of the following two episodes:

- pressurization or depressurization of alternately self-sealed and leaking hydrothermal fluid reservoir that traps volatiles exsolved from a crystallizing rhyolitic magma;
- movement, formation and crystallization of rhyolitic and/or basaltic magma.

Recent studies [Chang et al., 2007] drown the attention to a potential sill around 7-10 km below the surface of the caldera, where the expansion or reduction in the lava flow is linked to the continuous uplift and subsidence of the ground.

Even though there is not yet a definitive configuration of the super volcano underground dynamics, what is clearly evinced by the numerous studies is that a model that considers multiple sources of deformation is an appropriate fit for the complex Yellowstone volcanic system (Fig. 2).

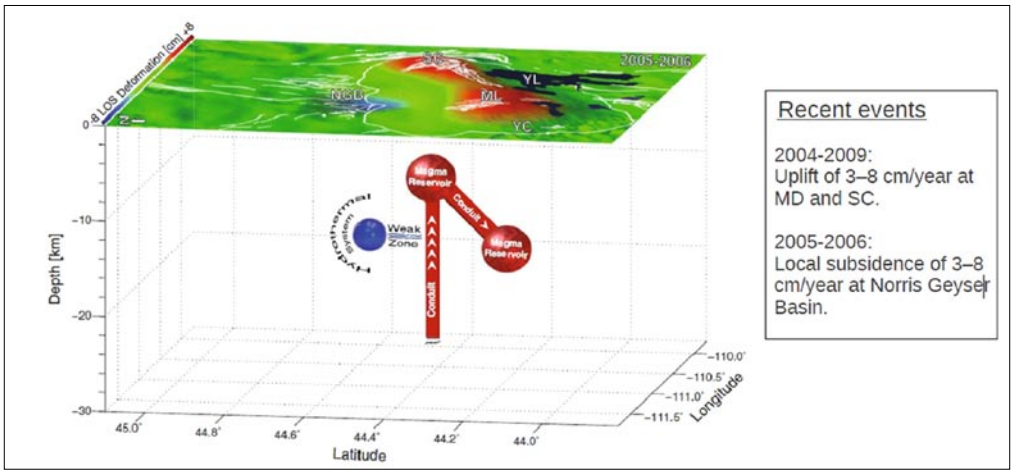

Figure 2 - Conceptual model for the Yellowstone deformation with Quaternary faults (white lines on the surface displacement map) and water bodies (black areas).

A strict continuous monitoring of the area is necessary to increase knowledge of the phenomena ongoing below the crust of the caldera and SAR images integrated with GPS measurements are still the best tools for this aim [Chang et al., 2010; Alymand Cochran, 2011]. Observations of cyclical Yellowstone crustal deformation are key to evaluating the hazards of this active volcanic system. Such data improve understanding of the relation between time dependent - deformation and magma migration and help differentiate between hydrothermal and magmatic sources.

SAR Interferometry

Interferometric synthetic aperture radar (InSAR) has become an important tool for measuring slow surface deformation associated with natural hazards such as earthquakes and volcanoes. Essentially, it is possible to: estimate topographic heights (Single-pass

Interferometry) and detect displacement (Repeat-pass Interferometry). The great advantage of SAR is that the observations are acquired with virtually complete spatial coverage, rather than the sparse observations inherent in conventional (including GPS) geodesy. In principle, all three components of surface displacement could be obtained from space; in practice, it is likely to obtain at most two, if data from both the ascending and descending passes of the satellite are available.

On the other hand, measurement of surface displacement with SAR interferometry depends on the nature of the surface change. In fact, the conditions under which SAR interferometry gives useful information on surface change is a major topic of current research. There are two important necessary conditions for detecting and measuring surface change with SAR:

- Changes between successive images must not be too large, specifically the displacement gradient across a pixel must fall within some value.
- The radar-scattering characteristics within each pixel must remain similar in the time between the two image acquisitions, specifically the root-mean-square (rms) position of the surface scatterers within a pixel must remain constant within a fraction, say 10 to 20%, of the radar wavelength.

The first condition is unlikely to pose significant problems, at least in theory. When it is violated because natural phenomena generate large displacements and displacement gradients (e.g., volcanic eruptions, landslides), simple differencing of before and after topographic data should be adequate to define the changes to the degree of accuracy required for their study. Of course, obtaining such topographic data may be quite challenging in a practical sense. The second condition is more problematic. When this condition is not met, it is termed temporal decorrelation, and it constitutes one of the major problems for SAR interferometry.

Correlation and coherence maps

Correlation, sometimes called coherence, is a standard measure of the statistical similarity of the phase of two SAR images. It describes the quality of the interferometric phase, consequently, how well motion signature can be isolated in an interferogram.

Theoretically, correlation ranges between 0 (no correlation) and 1 (perfect correlation). In practice, a number of pixels are weighed to estimate the correlation. A correlation of 0.5 marks a signal-to-noise ratio (SNR) of 1 in linear scale. When the correlation is higher than 0.20, phase information can be retrieved and becomes better when correlation increases; when correlation is between 0.15 and 0.20, it is possible but hard to retrieve some phase information; and when the correlation is below 0.15, no phase information can be retrieved. Generally, high correlation (> 0.20) is expected in areas where the surface condition does not change much with time, such as in urban areas, and low correlation is expected where vegetation is present.

The detailed theory and mathematical derivation of correlation can be found in several previous studies. Hereafter the relevant equations are presented. Assume that pixels of the complex radar images for first and second acquisition are [1]:

$$s_1 = c + n_1$$
$$s_2 = c + n_2 \quad [1]$$

where c is correlated part of the signal, and n_1 and n_2 are the uncorrelated noise caused by baseline, temporal, thermal, rotation, and other unknown factors. One measure of the correlation between two images is [2]:

$$\gamma = \frac{\left|\left\langle s_1 s_2^* \right\rangle\right|}{\sqrt{\left\langle s_1 s_1^* \right\rangle \left\langle s_2 s_2^* \right\rangle}} \quad [2]$$

where $s*$ is the complex conjugate of s, and $\langle\ \rangle\bullet$ denotes ensemble average, realized in practice by spatial averaging with a rectangular filter when the interferometric phase varies slowly. When the two radar images are exactly the same, correlation equals 1, and when they are completely different, the correlation approaches 0. Correlation is due to many more factors (thermal noise, image misregistration, geometrical, volumetric and temporal decorrelation) but in most cases the total coherence/correlation (γ) can be reduced to 3 terms: thermal, spatial and temporal [3]:

$$\gamma = \gamma_{thermal} \cdot \gamma_{spatial} \cdot \gamma_{temporal} \quad [3]$$

The thermal decorrelation is related to the SNR of the radar signal as [4]:

$$\gamma_{thermal} = 1/1 + SNR - 1 \quad [4]$$

In most cases, the SNR for ERS and ALOS is high enough to ignore this effect. Exceptions include special cases such as L-band over a sandy surface where the SNR is significantly lower. The spatial decorrelation is caused by the nonzero perpendicular baseline between the reference and repeat images. There are two effects of spatial decorrelation, namely: 1) volumetric decorrelation and 2) surface decorrelation. For area with high penetration, such as pine forests and ice, volume decorrelation dominates. However in our case, no significant volume decorrelation is observed, thus, we only consider spatial decorrelation related to surface scatterers. There are two ways to estimate the spatial decorrelation. One way is by using a range spectral filter, and the other way is by using the following model. If the satellite has a perpendicular baseline of B, the spatial correlation between the 2 radar images is [5]:

$$\gamma_{\text{spatial}} = 1 - 2\left|\mathrm{B}\right| \mathrm{Ry} \cos 2(\theta - \alpha) / \lambda\rho \quad [5]$$

where R_y is the range resolution, θ is the incidence angle, α is the local surface slope in range direction, λ is the wavelength, and ρ is the distance between the satellite sensor and the target on the surface. This equation is used to isolate the temporal decorrelation from

the measured decorrelation in the following analysis. When correcting spatial decorrelation using this equation, we need to make sure that no bandpass filtering is done during the processing.
The temporal decorrelation is caused by surface changes between the two acquisitions. Generally, temporal decorrelation increases with the amount of vegetation cover because the scatterers on the plants change with time. Other seasonal factors, such as snow, cultivation, erosion, deformation, affect decorrelation. With sufficiently high SNR and low volumetric decorrelation, temporal decorrelation can be isolated after removing the spatial decorrelation.
The phase noise can be estimated from the interferometric SAR pair by means of the local coherence. The local coherence is the cross-correlation coefficient of the SAR image pair estimated over a small window (a few pixels in range and azimuth), once all the deterministic phase components (mainly due to the terrain elevation) are compensated for. The deterministic phase components in such a small window are, as a first approximation, linear both in azimuth and slant-range. Thus, they can be estimated from the interferogram itself by means of well-known methods of frequency detection of complex sinusoids in noise (e.g. 2-D Fast Fourier Transform (FFT)). The coherence map of the scene is then formed by computing the absolute value of coherence on a moving window that covers the whole SAR image. The coherence value ranges from 0 (the interferometric phase is just noise) to 1 (complete absence of phase noise).

Data

Snow and Temperature data

The Natural Resources Conservation Service (NRCS) installs and maintains an extensive automated system (SNOwpack TELemetry or SNOTEL) designed to collect snowpack and related climatic data in the Western United States and Alaska.
The data, as well as related reports and forecasts, are available through an extensive Internet delivery system and other distribution channels.
In the Yellowstone area, SNOTEL stations are the only available free web source for snow depth and temperature historical values. The advantage of measuring both snow depth and temperature values in the same location yields to a better understanding of snow conditions relative to a certain height.
In Figure 3 the operating stations in the state of Wyoming are shown: even though the stations are wide spread all over the state the Yellowstone caldera (on the upper left side) is covered by only one station located at its edges (Canyon).
Consequently, data coming from stations located in Montana, close to the Yellowstone area, are also taken into account.
Four stations are considered for this study relating to the period 2006-2010: Canyon, West Yellowstone, Fischer Creek and North-East Entrance (Fig. 3).
The fifth station, Black Bear station in Montana, a few kilometers south of West Yellowstone station, has been later introduced since a second time span (from 1992 to 1996) needed to be considered and this station was close enough to the study area.
Since related to a different time period, its values of snow depth and temperature were considered separately. Since they are at different elevations, their measurements better represent the topography of the region.

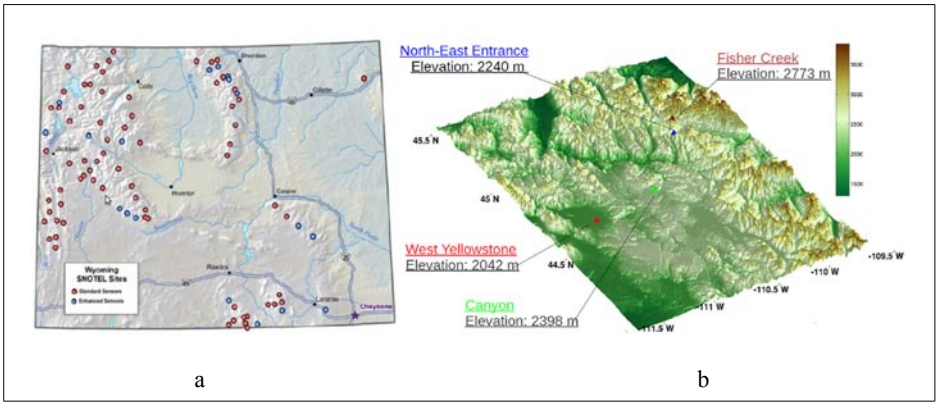

Figure 3 - SNOTEL stations (a) and four of the five selected stations referring to the 2006-2010 period (b).

The open source GMT (http://gmt.soest.hawaii.edu) has been used to plot both snow and air temperature data (Fig. 4). It is developed and maintained by P. Wessel and volunteers, supported by the National Science Foundation and released under the GNU General Public License.
In order to have a unique pattern across the whole Yellowstone area, the mean value of snow depth measurements has been calculated.
To plot the data a short script has been written.

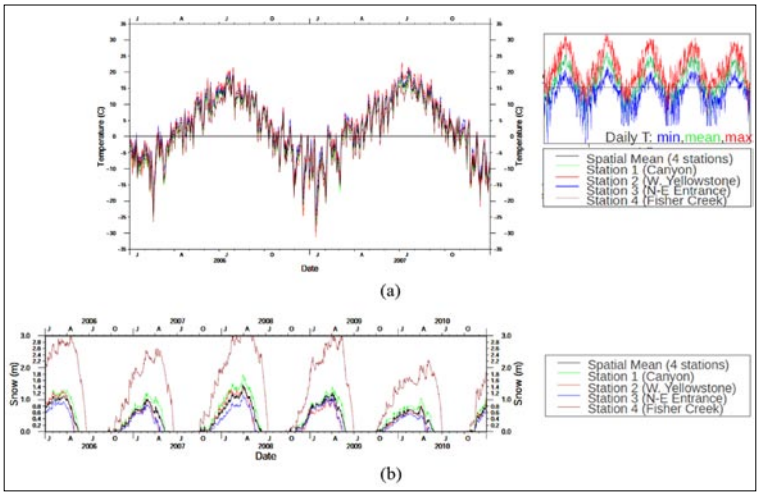

Figure 4 - SNOTEL stations data: daily Mean Temperature (a) and Snow Depth (b).

SAR data: ENVISAT, ERS1 and ALOS

This study aims to examine correlation maps of SAR interferograms generated from images acquired at C and L bands during different seasons and link coherence with snow coverage and temperature values.

Correlation, in favorable conditions, can last for more than one year and satellites are usually operative for as long as 5 to 10 years: to guarantee that a certain number of interferograms could be generated and compared, the time span of this study lasts almost 5 years, between 2006 and 2010. During this period, ENVISAT, ERS and ALOS satellites were operative.
Different SAR archives were used to download the data.
As part of Earthscope's GeoEarthscope project, UNAVCO university-governed consortium created an archive of SAR imagery (http://geoesinsar.unavco.org), with data supplied by the European Space Agency (ESA, ERS1, ERS2 and ENVISAT missions) and the Alaska Satellite Facility (ERS1, ERS2 and Radarsat1).
We selected for the ENVISAT mission a rectangular area from 44 to 45 degrees of latitude and from -111 to -110 degrees in longitude (Fig. 5).
The chosen date limit is between January 2006 and April 2010 when the expected satellite life span was ending. From the 4 tracks and 8 frames compatible with the search parameters only 2 tracks (41 and 320, one ascending and one descending) and 4 frames were covering most of the Yellowstone caldera.
To overcame missing data from ENVISAT images archive, available only for acquisitions during summer months, ERS1 data were collected in the time-span 1992-1996. Orbits traveled by ENVISAT are the same of ERS 1, with the same paths or tracks. Unluckily, track 320 have no winter acquisition in the period 1992-1996. Anyhow, some images were available from track 41 (Fig. 5) and downloaded from the UNAVCO archive (http://geoesinsar.unavco.org).

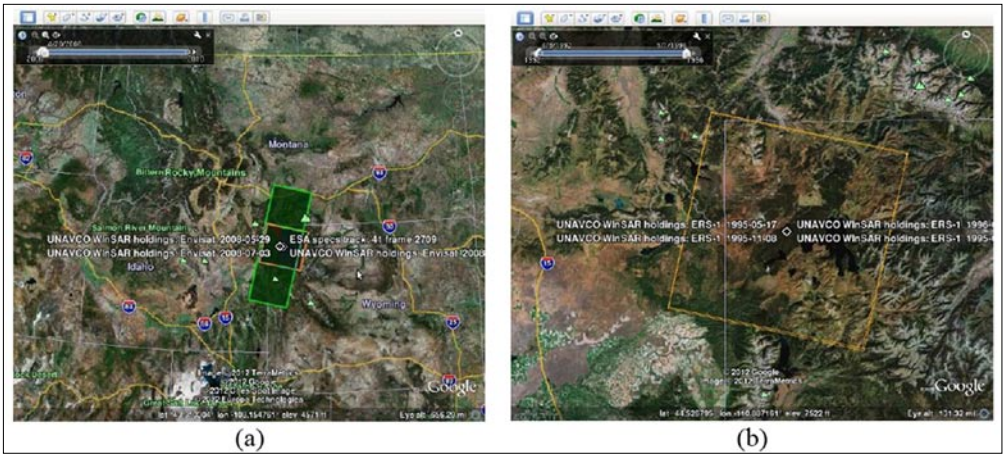

Figure 5 - Available ENVISAT (track 41, frames 2708-2709, a) and ERS1 images (track 41, frames 2709, b).

To perform additional comparisons with ERS1, ALOS data of the PALSAR sensor were downloaded (https://auig.eoc.jaxa.jp/auigs) with time span (2006-2010), operational mode (FBD, FBS) and off-nadir angle (larger than 30.8°). Acquisitions containing the entire area of the Yellowstone caldera are: path 528, frame 2720 (descending) and path 198, frame 880 (ascending) (Fig. 6).

Figure 6 - ALOS data on the Yellowstone caldera.

The first step in generating interferograms and correlation maps is to obtain as many images as possible covering the Yellowstone area between 2006 and 2010. To investigate different surface conditions the date of SAR acquisitions for each track and frame is plotted with the corresponding daily mean air temperature and snow depth value.

Table 1 - SAR acquisition period for the interferogram comparison.

IMAGE 1	IMAGE 2
summer	summer
winter	winter
autumn or spring	autumn or spring
summer	autumn or spring
winter	autumn or spring

Pairs of images with the shortest baseline (in order to minimize the contribution of spatial decorrelation) are chosen so that the following combination are represented for each satellite (Tab. 1).

Summer means no snow coverage and temperatures considerably above zero for more than a day in a row. Winter, at the contrary, means temperatures sensitively below zero for two or more days and snow coverage. Spring and autumn have temperatures slightly above zero and surface still covered with snow. Temporal baselines of the chosen pairs of SAR images can varies from few months to more than one year depending on the season.

What it is expected is that a good correlation is maintained for longer period when no significant variation on the ground surface occurs, for example between pairs of images acquired during summer months. Furthermore, previous studies shows how L-band can penetrate snow and keep coherence high even during winter months [Froger et al., 2004].

Interferograms and corresponding correlation maps are generated with the open source program GMTSAR and a first qualitative comparison is performed.
In order to analyze the same area in each correlation map, a subset common to all the frames is isolated. Consequentially, correlation values referring to exactly the same area can be compared as well as C-band and L-band differences in correlation can be analyzed.

Methodology

The SAR sensors ERS-1 (C-band,1992-96), ALOS (L-band) and ENVISAT (C-band, 2006-10) have been processed to measure ground deformations and study the decorrelation at C-band and L-band as a function of frozen and unfrozen conditions in the Yellowstone area.
To evaluate the deformation velocity field, GPS measurements were also taken into account even though GPS measurements lack the detailed spatial information that can recover using InSAR measurements. The technique used to measure displacements is the differential SAR interferometry: two complex SAR images, acquired at different times but with the same incident angle (ca. 23°) are used to generate an interferogram where each pixel represents a delta in phase between the two acquisitions (repeat pass approach). Subsequently a DEM (Digital Elevation Model) is used to correct the generated interferogram. The short baseline of the chosen pairs assures an irrelevant influence in the inaccuracy of the DEM used for the topographic corrections. Only images acquired during the summer months are selected in order to reduce the decorrelation due to snow cover. The obtained interferograms are unwrapped to convert the cyclic phase values to continuous values. Once interferograms are formed, they are compared to evaluate the presence of atmospheric artifacts, using the method of Massonnet and Feigl [1995]. Hence, some interferograms are discarded and part of the remaining ones, showing a constant deformation velocity field, are stacked. Since deformations can be calculated along the line of sight of the satellite, both ascending and descending orbits are used to obtain the vertical and lateral components of the deformation field. The velocity vectors are assumed to radiate from two central axes centered on the two structural domes in the Yellowstone caldera.Vertical displacements can be measured using InSAR at a much better accuracy than lateral displacements. The northing displacement is always the least accurately resolved component due to lack of diversity in the viewing geometry of near-polar orbiting satellites such as ERS and ENVISAT. SAR pairs with different incident angles allows a more precise assessment of the error and more accurate measurements of lateral displacement. Unfortunately not many pairs with these characteristics were available for the used satellites.

SAR interferometry and coherence maps

SAR data are processed with the open source GMTSAR, developed by Sandwell et al. [2011], with three main components:

- a preprocessor for each satellite data type (e.g., ERS, Envisat, and ALOS) to convert the native format and orbital information into a generic format,
- an InSAR processor to focus and align stacks of images, map topography into phase and form interferogram
- a postprocessor, mostly based on GMT, to filter the interferogram and construct interferometric products of phase, coherence, phase gradient and line of sight

displacement in both radar and geographic coordinates.
In order to choose pairs of images and form interferograms, it is important to know the spatial baseline separating each acquisition. The shortest the baseline, the lowest the geometric decorrelation.

ENVISAT baseline and processing
Once GMTSAR has calculated the values of perpendicular baselines, they are plotted with time, temperature and snow depth values thanks to GMT (Fig. 7). Figure 7 shows the ENVISAT data labeled with orbit numbers: the blue line represents the snow depth and the green one is the daily mean temperature. Acquisitions are concentrated during summer and spring/autumn months and no winter images are available for both tracks. Perpendicular baseline ranges between few meters to almost 1400 m, exceeding the value of the critical baseline: a perpendicular baseline around or bigger than 1100 m shouldn't be considered for ENVISAT interferogram generation, to avoid significant correlation losses. Thanks to this consideration, pairs of SAR images are chosen and underlined with pink/grey lines.

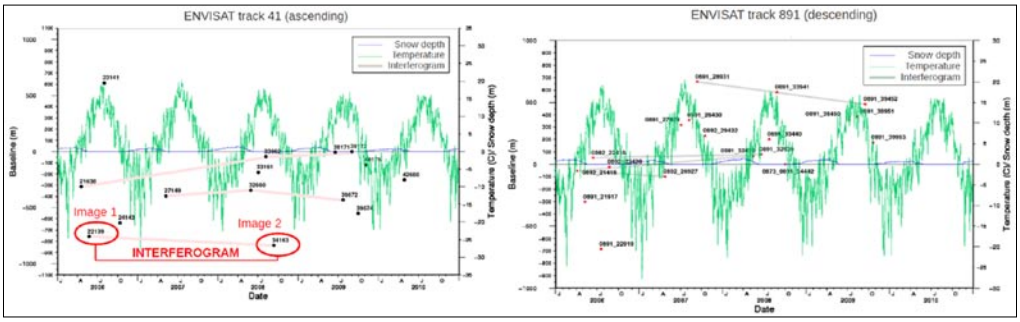

Figure 7 - C-band analysis: ENVISAT data plotted with time, temperature and snow depth.

Before starting the InSAR processing, a Digital Elevation Model (DEM) covering an area wider than the image frames must be generated. This can be done following the link: http://topex.ucsd.edu/gmtsar/demgen/. Two DEM has been generated for track 41, frame 2709 (Fig. 9, left) and for track 320, frame 891 (Fig. 9, right).
Some parameters are set for pre-processing, focusing and aligning Single Look Complex (SLC) images, for making and filtering interferograms, phase unwrapping and geocoding. Starting from the raw and topographic data (DEM) different outputs have been so generated: amplitude and correlation maps, wrapped and unwrapped interferograms (Fig. 8) with radar or longitude-latitude coordinates.Color fringes indicate changes in the radar range (one color cycle corresponding to 2.8 cm of line-of-sight displacement). Moreover .kml files for Google Earth visualization are generated.

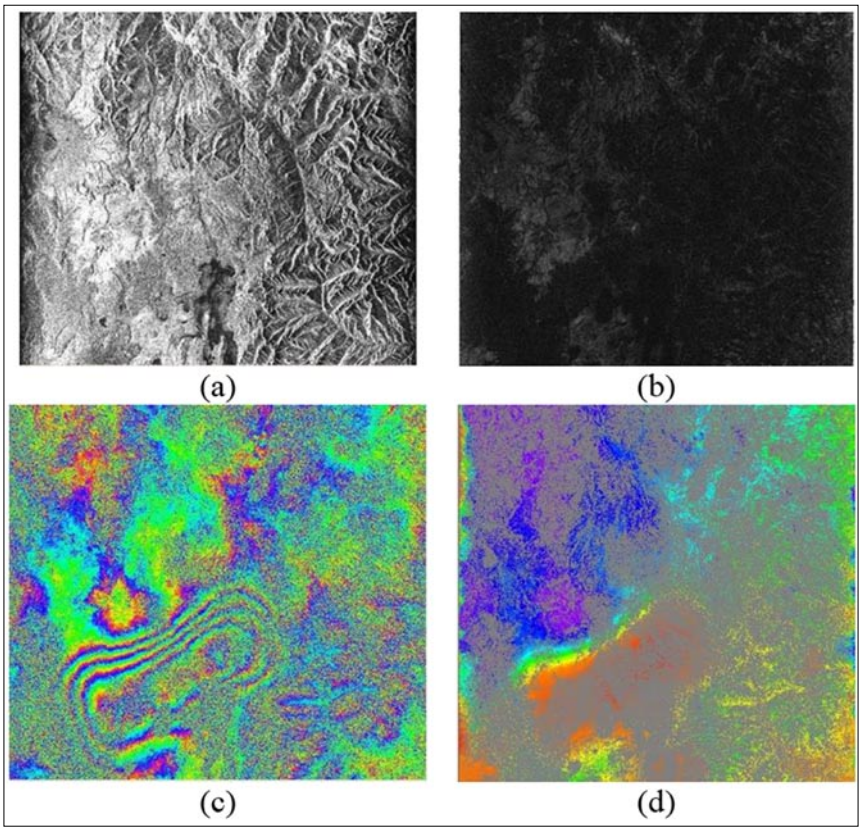

Figure 8 - C-band analysis: ENVISAT Amplitude (a), Correlation map (b), Wrapped (c) and unwrapped (d) interferograms.

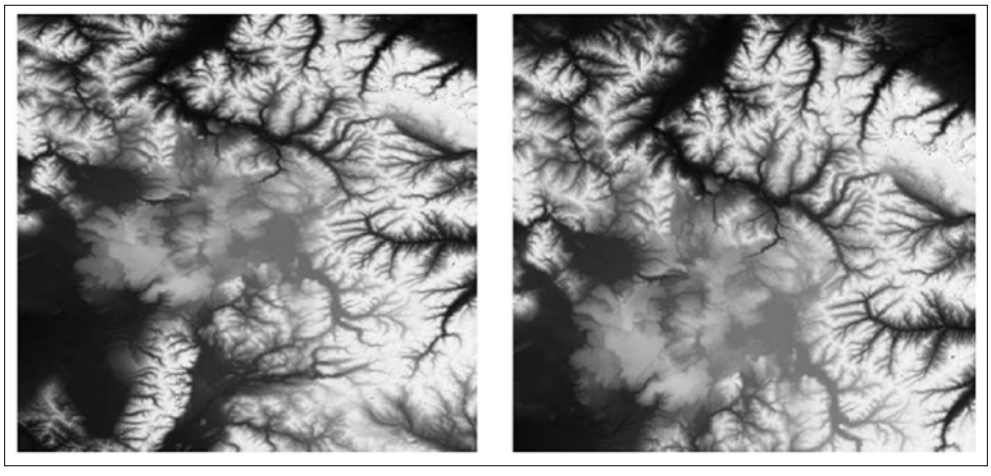

Figure 9 - DEM for track 41, frame 2709 (left) and DEM for track 320, frame 891 (right).

ALOS baseline and processing

As for ENVISAT data, perpendicular baseline of ALOS images have been calculated. Output files comprehend a plot with a graphical representation of the relative position between acquisitions and a data file with perpendicular and parallel baseline values. A plot comprehensive of time of acquisition, temperature and snow depth is generated with GMT for ALOS tracks 198 and 528 (Fig. 10). ALOS acquisitions are concentrated during winter months. Baseline can be as long as 5 km but, in this case, the critical value is much bigger than the ENVISAT one. For the Fine-Beam Single polarization (FBS) mode the baseline should not be larger than 13.1 km whereas the for Fine-Beam Dual polarization (FBD) images the critical value is 6.5 km. Hence, no restrictions due to critical value of the baseline apply here. Chosen pairs of SAR images are underlined with pink/grey lines (Fig. 10).

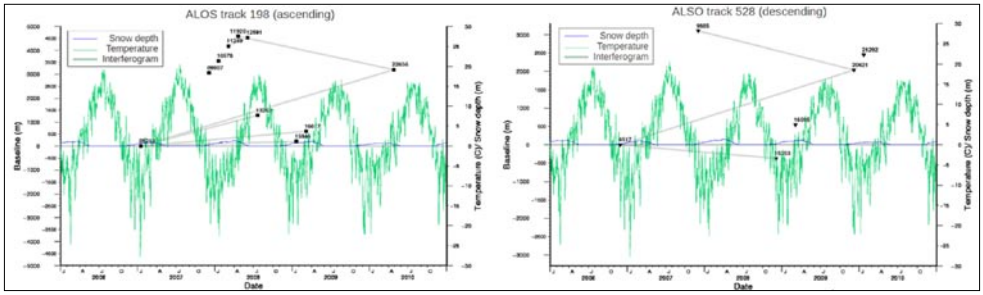

Figure 10 - L-band analysis: ALOS data plotted with time, temperature and snow depth.

Images to form an interferogram can be chosen in either FBD or FBS mode. If one image is FBS, it has to be the master: the program will perform an upsampling of the FBD image, characterized by a lower resolution. Again, as done with ENVISAT data, Digital Elevation Models are generated for track198 and track 528 (Fig. 12) and used to produce similar output files (Fig. 11). Default values have not been modified in the configuration files.
Color fringes indicate changes in the radar range. One color cycle corresponding 11.8 cm of line-of-sight displacement.
Correlation map shows correlation as a function of brightness: areas in black represent very low correlation whereas bright areas have higher correlation.
Confronting available ALOS and ENVISAT data in one plot highlights how acquisitions between L-band and C-band are complementary: winter SAR data find no equivalent ENVISAT acquisitions (Fig. 13).

ERS1 baseline and processing

The introduction of ERS1 data is fundamental to compare results from C-band and L-band with the same surface conditions. Baseline values are again plotted with temperature and snow depth data (Fig. 13).
ERS1 images integrate ENVISAT missing data from winter months. Pairs are chosen in order to create winter to winter or winter to spring/autumn interferograms.
Baseline values must be smaller than 1.2 km even though best results can be obtained with a baseline length near 200 m. Only two pairs of images go beyond this value with a length close respectively to 300 and 600 m (Fig. 14).

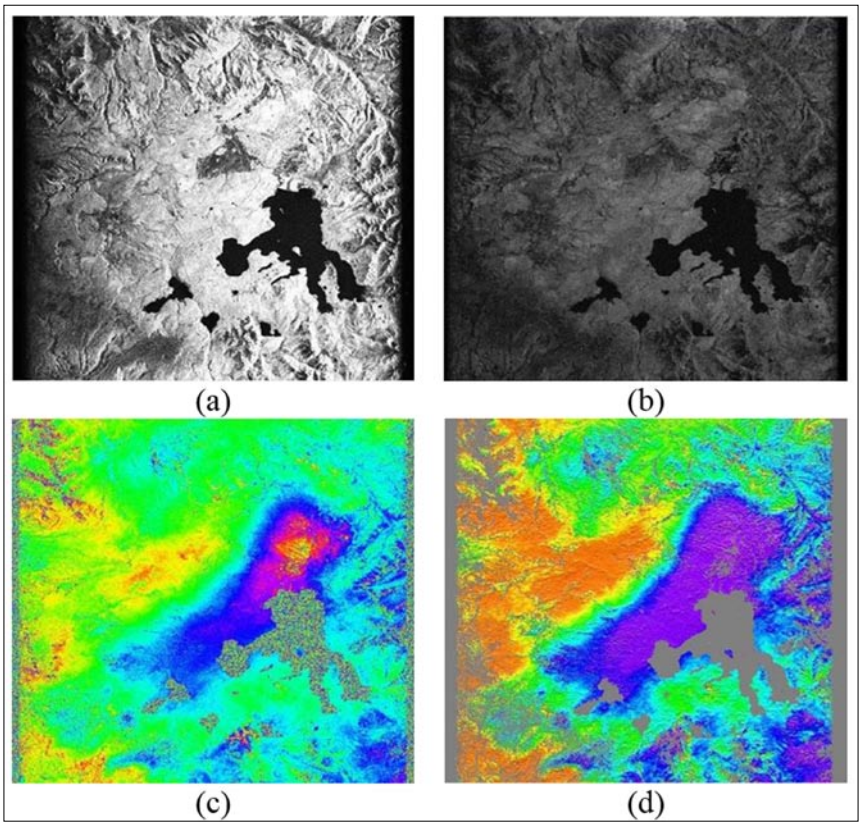

Figure 11 - L-band analysis: ALOS Amplitude (a), Correlation map (b), Wrapped (c) and unwrapped (d) interferogram.

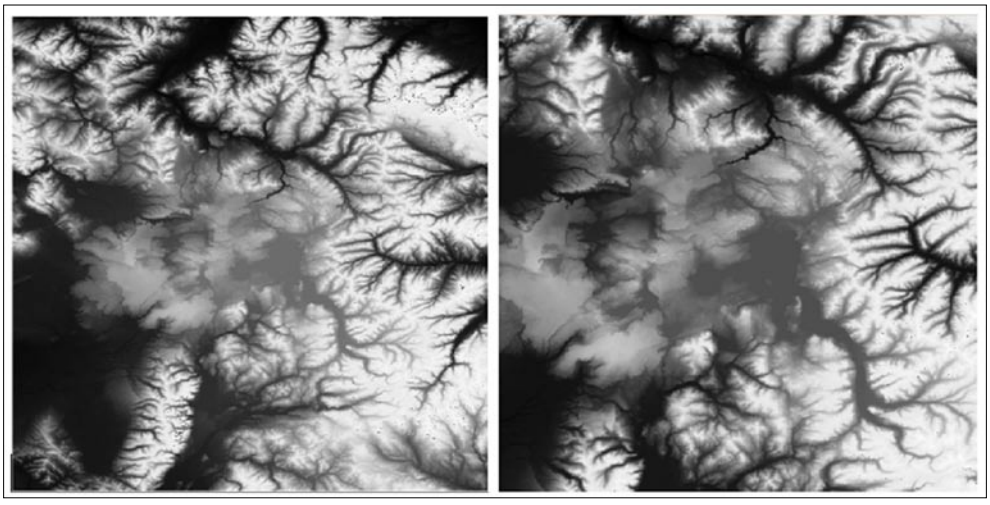

Figure 12 - DEM for track 198 (left) and DEM for track 528 (right).

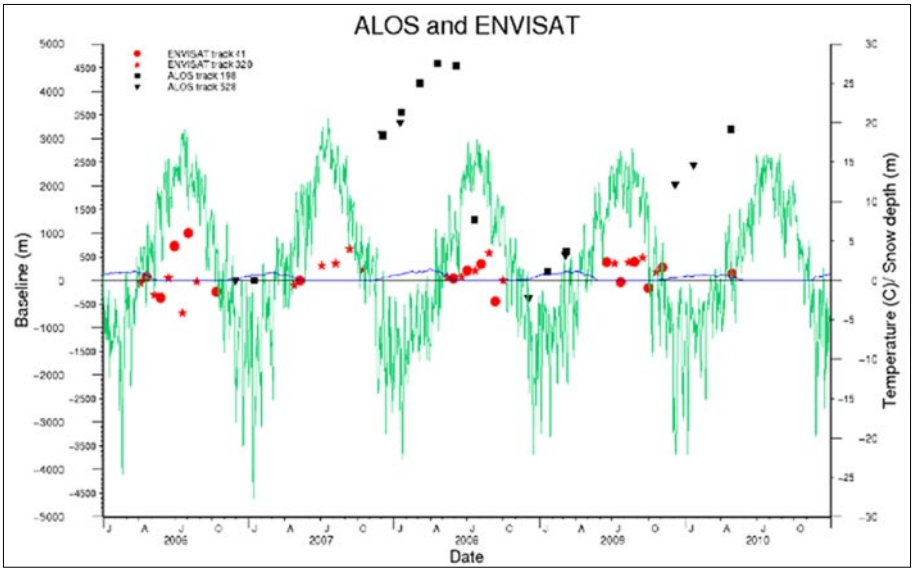

Figure 13 - L-band and C-band analysis: ALOS and ENVISAT track comparison.

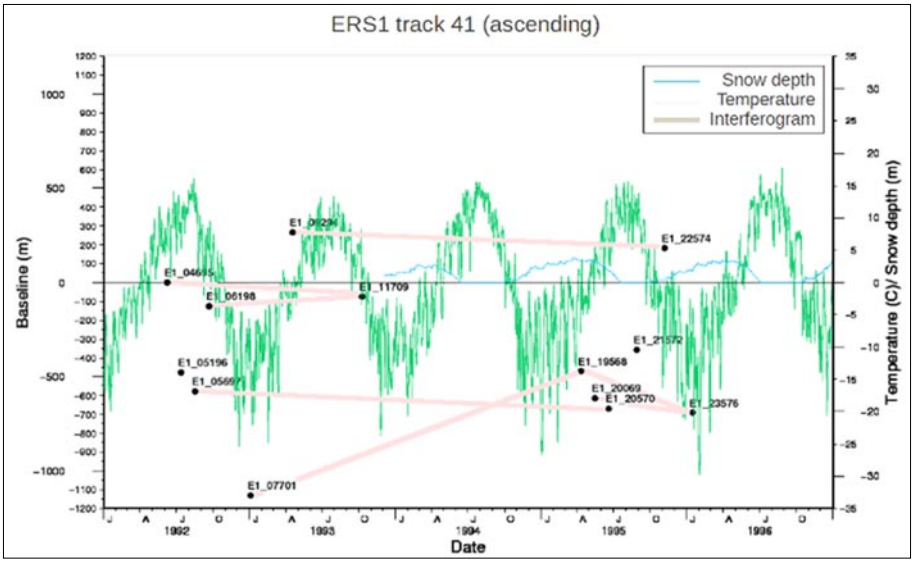

Figure 14 - C-band analysis: ERS1 data plotted with time, temperature and snow depth.

A new DEM is not necessary because the one generated for ENVISAT track 41 covers the same area of ERS1 track 41. The ERS1 images are processed and the output are shown in Figure 15. Each phase fringe is directly related to the radar wavelength (5.6 cm for ERS satellites) and represents a displacement relative to the satellite of only half the above wavelength (28 mm).

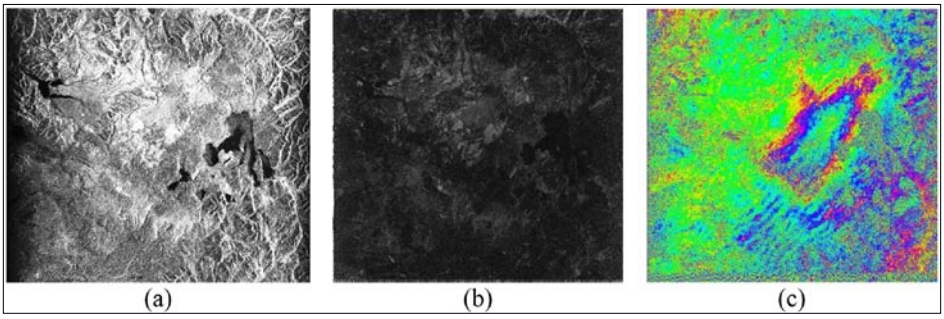

Figure 15 - C-band analysis: ERS1 Amplitude (a), Correlation map (b) and Interferogram (c).

Around 30 interferograms has been processed totally, linking coherence to snow coverage and temperature values. Default settings have been used for processing. Examples are shown in Figure16. If average correlation is lower than 0.2 phase unwrapping is skipped in GMTSAR. In fact, in most cases there is a critical range of correlation between 0.15 and 0.20 that determines whether an interferogram is usable. When the correlation is larger than 0.20, phase information can be retrieved and becomes better when correlation increases; when correlation is between 0.15 and 0.20, it is possible but hard to retrieve some phase information and when the correlation is below 0.15, no phase information can be retrieved.

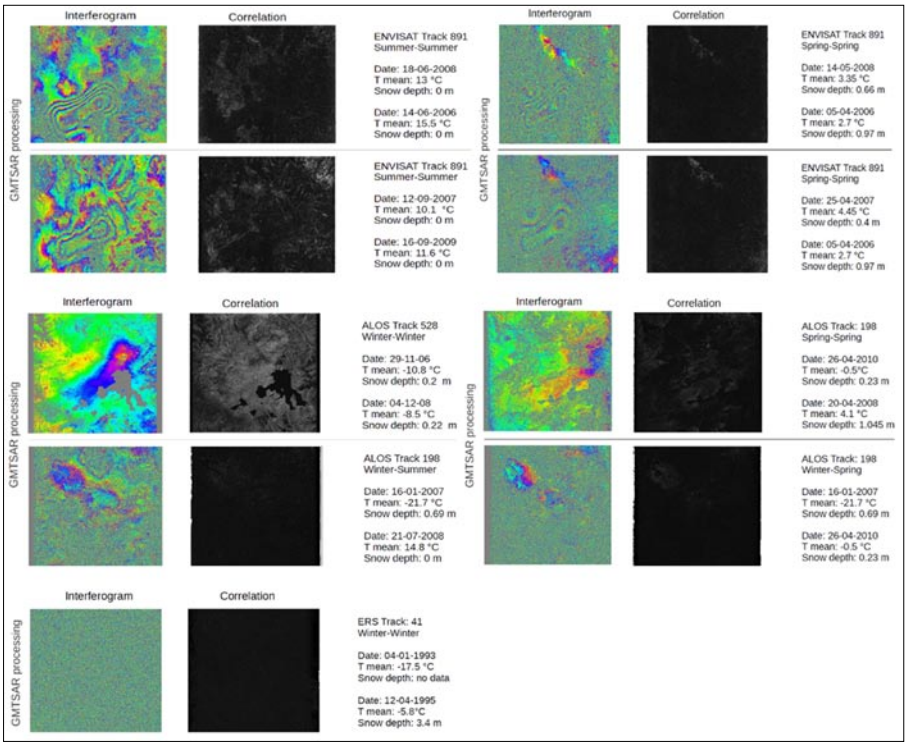

Figure 16 - C-band and L-band analysis.

Conclusions

The interpretation of ground deformations due to the active volcanic system below the caldera floor can take great advantage of SAR measurements: thanks to the interferometric tool and the integration and support of punctual but continuous GPS measurements is possible to quantify deformation and deformation velocity fields in the Yellowstone caldera and its surroundings.

From these measurements, besides the direct information, also other important parameters can be evaluated: for instance, the inflated volume during an uplift episode or the deflating volume in the opposite case. One of the main limitations of the InSAR technique is temporal decorrelation due to surface change, particularly in vegetated areas, because the low correlation prevents the recovery of the phase measurement.

Aim of this study is to examine correlation maps of SAR interferograms generated from images acquired at C and L band during different seasons and link coherence to snow coverage and temperature values.

To isolate temporal decorrelation, pairs of images with the shortest baseline are preferably chosen. Correlation maps are analyzed in relation to snow depth and temperature.

Results obtained with ENVISAT and ERS satellites (C band) are later compared with the ones from ALOS (L-band).

The study shows how a longer wavelength perform better during winter time, when the surface is covered with snow and temperature is below zero (Tab. 2). Both satellites, though, have a bad attitude towards wet snow: especially during spring and fall, coherence is so low that no information about phase can be retrieved. During summer months both L- band and C-band maintain a good coherence with L- band performing better over vegetated areas, supporting the result of previous studies [Sandwell et al., 2011].

Table 2 - Experimental Results.

	winter to winter (snow, T<0)	**summer to summer (no snow, T>0)**	**summer to winter ($snow_1$>0, $snow_2$=0)**	**spring to autumn (mixed conditions)**
ALOS L-band	**correlation**	no correlation	no correlation	low correlation phase unwrapped locally with snow and T_1>0, T_2<0
ENVISAT C-band	no data	**correlation**	no correlation	low correlation
ERS1 C-band	no correlation	**correlation**	no correlation	low correlation phase unwrapped locally with snow and T_1>0, T_2<0

References

Aly M.H., Cochran E.S. (2011) - *Spatio-temporal evolution of Yellowstone deformation between 1992 and 2009 from InSAR and GPS observations.* Bulletin of Volcanology, 73(9): 1407-1419. doi: http://dx.doi.org/10.1007/s00445-011-0483-y.

Burgmann R., Rosen P.A., Fielding E.J. (2000) - *Synthetic aperture radar interferometry*

to measure Earth's surface topography and its deformation. Annual Review of Earth and Planetary Sciences, 28: 169-209. doi: http://dx.doi.org/10.1146/annurev.earth.28.1.169.

Carter A.J., Ramsey M.S. (2009) - *ASTER- and field-based observations at Bezymianny Volcano: Focus on the 11 May 2007 pyroclastic flow deposit*. Remote Sensing of Environment, 113: 2142-2151. doi: http://dx.doi.org/10.1016/j.rse.2009.05.020.

Chang W.L., Smith R.B., Wicks C., Farrell J., Puskas C.M. (2007) - *Accelerated uplift and magmatic intrusion of the Yellowstone caldera, 2004 to 2006*. Science, 318: 952–956. http://dx.doi.org/10.1126/science.1146842.

Chang W.L., Smith R.B., Farrell J., Puskas C.M. (2010) - *An extraordinary episode of Yellowstone caldera uplift, 2004–2010, from GPS and InSAR observations*. Geophysical Research Letters, 37 (23): L23302.

Di Martino G., Iodice A.,Riccio D., Ruello G. , Zinno I. (2012) - *On the fractal nature of volcano morphology detected via SAR image analysis: the case of Somma–Vesuvius Volcanic Complex*. European Journal of Remote Sensing, 45: 177-187. doi: http://dx.doi.org/10.5721/EuJRS20124517.

Dzurisin D. (2006) - *Volcano Deformation. Geodetic Monitoring Techniques*. New York, Springer-Praxis. doi: http://dx.doi.org/10.1007/978-3-540-49302-0.

Froger J., Fukushima Y., Briole P., Staudacher T., Souriot T., Villeneuve N. (2004) - *The deformation field of the August 2003 eruption at Piton de la Fournaise, Reunion Island, mapped by ASAR interferometry*. Geophysical Research Letters, 31: 14, L14601. doi: http://dx.doi.org/10.1029/2004GL020479.

Fukushima Y., Cayol V., Durand P. (2005) - *Finding realistic dike models from interferometric synthetic aperture radar data: The February 2000 eruption at Piton de la Fournaise*. Journal of Geophysical Research, 110: B03206. doi: http://dx.doi.org/10.1029/2004JB003268.

Lu Z., Wicks C., Dzurisin D., Thatcher W., Freymueller J.T., McNutt S.R., Mann D. (2000) - *Aseismic inflation of Westdahl Volcano, Alaska, revealed by satellite radar interferometry*. Geophysical Research Letters, 27 (11): 1567-1570. doi: http://dx.doi.org/10.1029/1999GL011283.

Massonnet D., Briole P., Arnaud A., (1995) - *ETNA monitored by spaceborne radar interferometry*. Nature, 375: 567-570. doi: http://dx.doi.org/10.1038/375567a0.

Massonnet D., Sigmundsson F. (2000) - *Remote sensing of volcano deformation by radar interferometry from various satellites.* in Remote Sensing of Active Volcanism (Eds Mouginis-Mark P.J., Crisp J.A. and Fink J.H.), American Geophysical Union, Washington, D. C. doi: http://dx.doi.org/10.1029/GM116p0207.

Massonnet D., Feigl K.L. (1995) - *Discriminating geophysical phenomena in satellite radar interferograms*. Geophysical Research Letters, 22 (12): 1537-1540. http://dx.doi.org/10.1029/95GL00711.

Massonnet D., Feigl K.L. (1998) - *Radar interferometry and its application to changes in the Earth's surface*. Reviews of Geophysics, 36 (4): 441-500. doi: http://dx.doi.org/10.1029/97RG03139.

Meertens C.M., Smith R.B. (1991) - *Crustal deformation of the Yellowstone caldera from first GPS measurements: 1987-1989*. Geophysical Research Letters, 18 (9): 1763-1766. doi: http://dx.doi.org/10.1029/91GL01470.

Pelton J.R., Smith R.B. (1982) - *Contemporary vertical surface displacements in Yellowstone National Park*. Journal of Geophysical Research: Solid Earth, 87: 2745-2761.

Puskas C.M., Smith R.B., Meertens C.M., Chang W.L. (2007) - *Crustal deformation of the Yellowstone-Snake River Plain volcano tectonic system: Campaign and continuous GPS observations, 1987–2004*. Journal of Geophysical Research, 112: B03401. doi: http://dx.doi.org/10.1029/2006JB004325.

Ramsey M.S., Flynn L.P. (2004) - *Strategies, insights, and the recent advances in volcanic monitoring and mapping with data from NASA's Earth Observing System*. Journal of Volcanology and Geothermal Research, 135 (1-2): 1-11. doi: http://dx.doi.org/10.1016/j.jvolgeores.2003.12.015.

Rosen P.A., Hensley S., Joughin I.R., Li F.K., Madsen S.N., Rodriguez E., Goldstein R.M. (2000) - *Synthetic aperture radar interferometry*. Proc. IEEE 88 (3): 333-382. doi: http://dx.doi.org/10.1109/5.838084.

Rothery D.A., Coppola D., Saunders C. (2005) - *Analysis of volcanic activity patterns using MODIS thermal alerts*. Bulletin of Volcanology, 67: 539-556. doi: http://dx.doi.org/10.1007/s00445-004-0393-3.

Sandwell D., Mellors R., Tong X., Wei M., Wessel P. (2011) - *Open radar interferometry software for mapping surface deformation*. Eos Transactions American Geophysical Union, 92 (28): 234. doi: http://dx.doi.org/10.1029/2011EO280002.

Smith R.B., Siegel L. (2000) - *Windows into the Earth: The Geologic Story of Yellowstone and Grand Teton National Parks*. Oxford University Press, New York, pp: 100-147

Wei M., Sandwell D.T. (2010) - *Decorralation of L-Band and C-Band Interferometry Over Vegetated Areas in California*. Geoscience and Remote Sensing, IEEE Transactions, 48(7): 2942-2952. doi: http://dx.doi.org/10.1029/2011EO280002.

Wicks C., Thatcher W., Dzurisin D., Svarc J. (2006) - *Uplift, thermal unrest, and magma intrusion at Yellowstone caldera, observed with InSAR*. Nature, 440: 72-75. doi: http://dx.doi.org/10.1038/nature04507.

Zebker H., Amelung F., Jonsson S. (2000) - *Remote sensing of volcano surface and internal processes using radar interferometry*. In Remote Sensing of Active Volcanism (Eds. Mouginis-Mark P.J., Crisp J.A. and Fink J.H.), American Geophysical Union, Washington, D. C.: AGU, pp. 179-205.